Supporting Online Materials for

Giant electrical modulation of magnetization in $Co_{40}Fe_{40}B_{20}$/ $Pb(Mg_{1/3}Nb_{2/3})_{0.7}Ti_{0.3}O_3$(011) heterostructure

Sen Zhang[1,2*], Yonggang Zhao[1,3*], Xia Xiao[4], Yizheng Wu[4], Syed Rizwan[5], Lifeng Yang[1], Peisen Li[1], Jiawei Wang[1], Meihong Zhu[1], Huiyun Zhang[1], Xiaofeng Jin[4] & Xiufeng Han[5]

[1]*Department of Physics and State Key Laboratory of Low-Dimensional Quantum Physics, Tsinghua University, Beijing 100084, P. R. China*

[2]*College of Science, National University of Defense Technology, Changsha 410073, P. R. China*

[3]*Collaborative Innovation Center of Quantum Matter, Beijing 100084, P. R. China*

[4]*Department of Physics, State Key Laboratory of Surface Physics and Advanced Materials Laboratory, Fudan University, Shanghai 200433, P. R. China*

[5]*Beijing National Laboratory for Condensed Matter Physics, Chinese Academy of Sciences, Beijing 100190, P. R. China*

*Correspondence and requests for materials should be addressed to Y. Z. (ygzhao@tsinghua.edu.cn) and S. Z. (zhangsen@nudt.edu.cn)

The spontaneous polarizations and X-ray diffraction patterns of PMN-PT with rhombohedral phase in (001)-cut and (011)-cut cases.

The spontaneous ferroelectric polarizations of PMN-PT with rhombohedral (R) phase are along the <111> directions[1], i.e. the body diagonals of the pseudo-cubic unit cell in the (001)-cut case [Fig. S1(a)]. While in the (011)-cut case, the spontaneous polarizations lie along the diagonals of the (011) and (01-1) plane, as shown in Fig. S1(b). The transition of coordinate axes between the (001)-cut case and (011)-cut case is also shown in Fig. S1(a), from which one can easily understand the relative orientation of the spontaneous polarizations in the (011)-cut case. The X-ray diffraction patterns of the (001)-cut and (011)-cut PMN-PT substrates are shown in Figs. S1(c) and S1(d), and the out-of-plane lattice parameters of the (001)-cut and (011)-cut cases can be deduced as 4.022 Å and 2.843 Å, respectively.

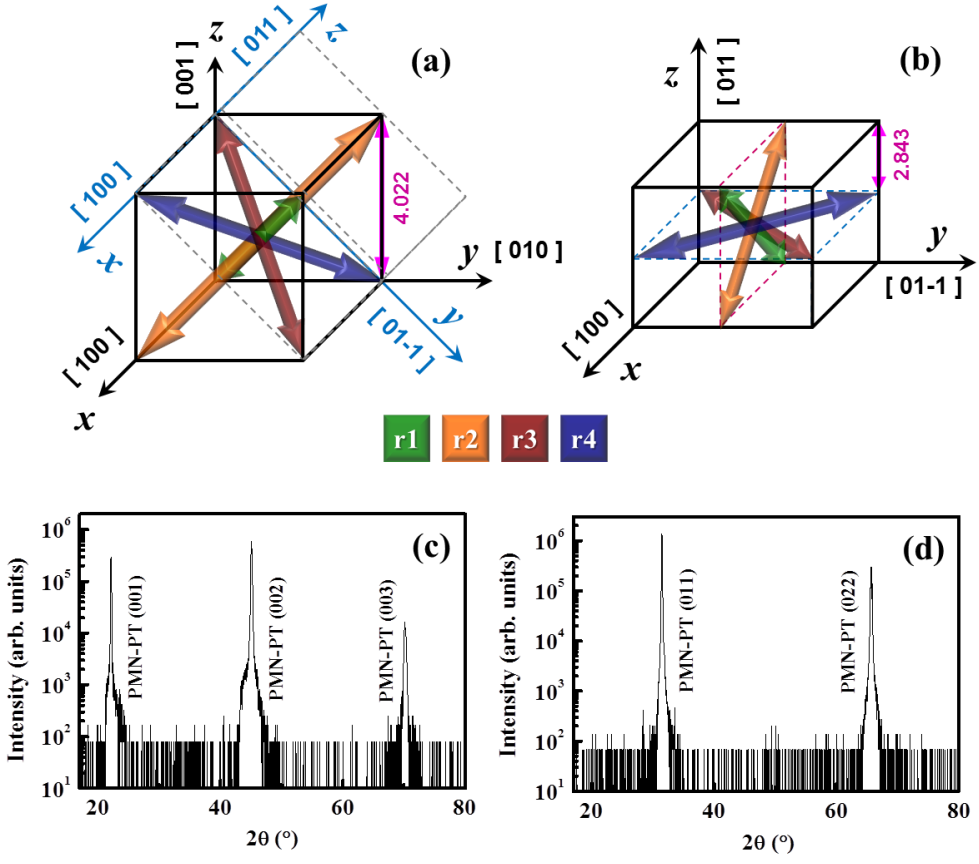

Figure S1 | Spontaneous polarizations and X-ray diffraction patterns of PMN-PT with the rhombohedral phase in the (001)-cut and (011)-cut cases. (a) The unit cell and

spontaneous polarizations of (001)-orientated PMN-PT. (b) The unit cell and spontaneous polarizations of (011)-orientated PMN-PT. (c) X-ray diffraction pattern of (001)-orientated PMN-PT substrate. (d) X-ray diffraction pattern of (011)-orientated PMN-PT substrate.

Condition optimization to enhance the electric-field controlled magnetization modulation.

In order to confirm and optimize the electric-field controlled giant magnetization modulation, more samples were prepared and measured, and similar behavior was shown with enhanced effect. Figure S2 shows the electric-field control of magnetization of Sample 2# along the [100] direction. From Fig. S2(a), one can see that the behaviors of M-H curves under electric fields of 0 kV/cm, 10 kV/cm and 20 kV/cm are almost the same as that of Sample 1# (i.e. Fig. 2(a) in the paper). What's more, one can see the obvious difference between the initial magnetic state (i.e. M-H at 0 kV/cm) and electrically poled magnetic state (i.e. M-H at 2^{nd} 0 kV/cm) from the expanded view of M-H curves [Figure S2(b)], which indicates that the magnetic anisotropy induced by domain reorientation after poling (Figure 1(e) in the paper), enhances the squareness and remnant magnetization along the [100] direction. From the inset of Figure S2(a), one can also see that the calculated relative magnetization change ($\Delta M/M$) is larger at lower magnetic fields. Hence, compared with the result in the paper [$\Delta M/M \sim 83$ % at 5 Oe, as shown in Fig. 2(c)], reducing the bias magnetic field increases $\Delta M/M$ [~ 90 % at 3 Oe, as shown in Fig. S2(c)] and increasing the bias magnetic field decreases $\Delta M/M$ [~ 63 % at 10 Oe, as shown in Fig. S2(d)].

However, further reducing the bias magnetic field can't always increase $\Delta M/M$, but would vanish it because the anisotropic strain induced easy axis of magnetization gives two equivalent directions, i.e. [100] and [-100] directions at zero electric field [Figure S3(a)] and [01-1] and [0-11] directions at large electric fields [Figure S3(b)]. For the M-E measurement along the [100] direction without bias magnetic field, the magnetization vector can be either

along the [100] direction or the [-100] direction at zero electric field, resulting in zero net magnetization and hardly any change in M-E curve [Figure S3(c)]. While for M-E measurement with a bias magnetic field, the magnetization vector can be only along the [100] direction at zero electric field and the change in M-E curve is obvious [Figure S3(d)].

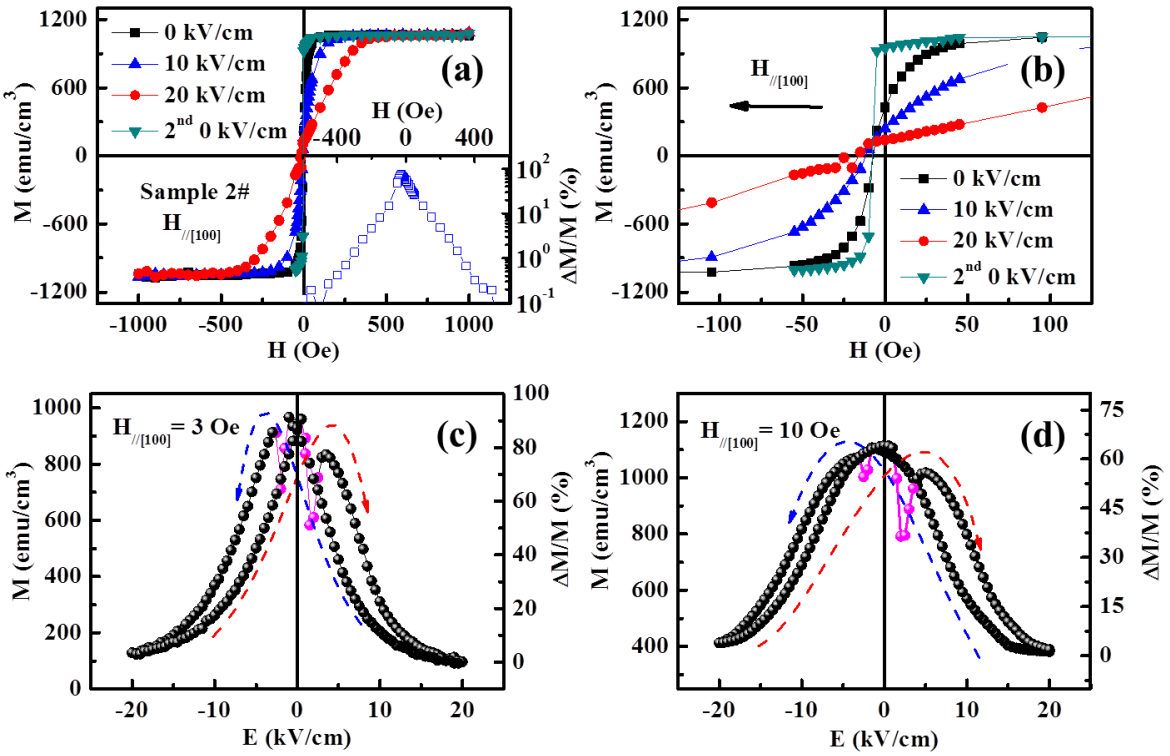

Figure S2 | Electric field control of magnetization of Sample 2# along the [100] directions. (a) Magnetic hysteresis loops measured along the [100] direction under electric fields of 0 kV/cm (square), 10 kV/cm (upward triangle), 20 kV/cm (circle) and after removal of the electric field (i.e. 2nd 0 kV/cm, downward triangle). Inset of (a) shows the calculated maximum relative magnetization change (ΔM/M, open square) at different magnetic fields. (b) The expanded region of M-H curves at low magnetic fields, in which the differences of squareness and remnant magnetizations among different M-H curves are more obvious. (c) Electric-field control of magnetization (sphere) measured along the [100] direction with an optimized magnetic field of 3 Oe. (d) Electric-field control of magnetization (sphere) measured along the [100] direction with a larger magnetic field of 10 Oe.

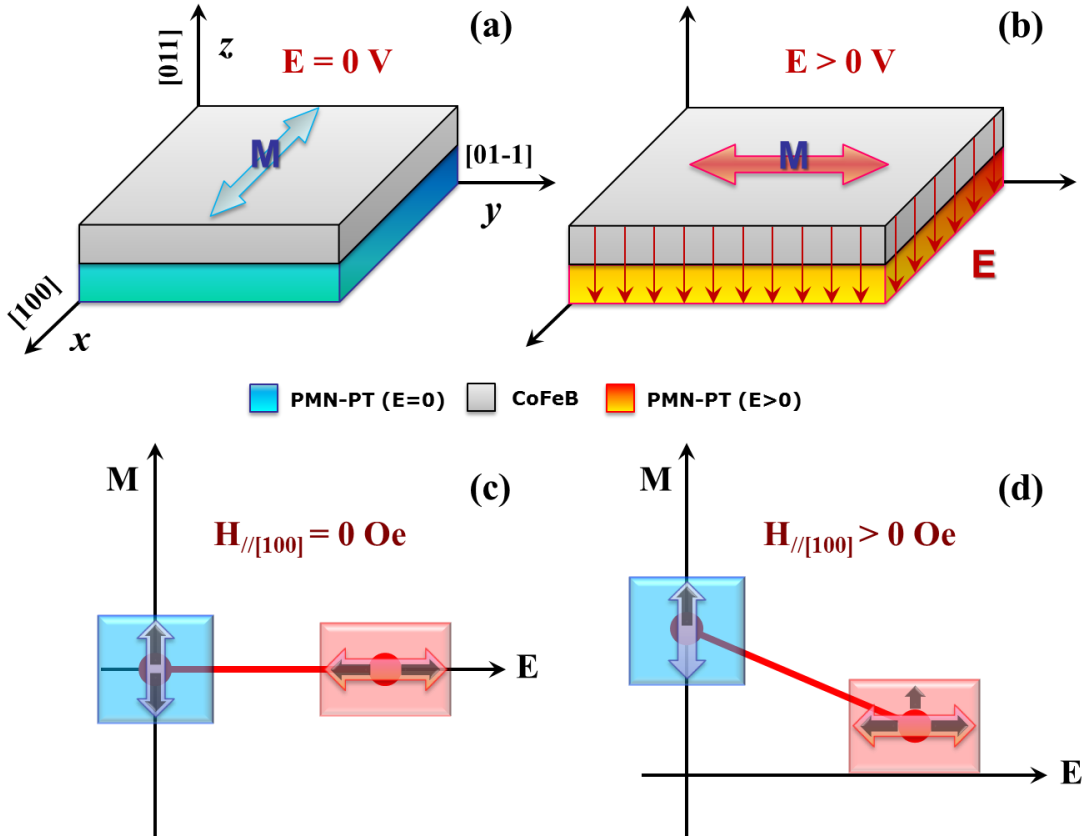

Figure S3 | The importance of bias magnetic field in the measurement of M-E curves. (a) Magnetic easy axis of the sample without electric field. (b) Magnetic easy axis of the sample under electric fields. (c) Sketch of M-E curve (red line), induced easy axes (board bidirectional arrows) and magnetization vectors (board unidirectional arrows) without magnetic field. (d) Sketch of M-E curve, induced easy axes and magnetization vectors with bias magnetic field along the [100] direction.

Investigation of the *anomalous* points and polarization reversal process of the (011)-orientated PMN-PT.

In order to explore the origin of the *anomalous* data points shown in Fig. 2(c) in the paper, M-E measurement under low electric fields (3 ~ 6 kV/cm) was carried out. After poling with a large negative electric field, the M-E curve of the sample was measured with a small increment of electric field (0.1 kV/cm) under a bias magnetic field of 5 Oe. During the M-E

measurement, the polarization switching ratio (PSR) was also acquired simultaneously by integrating the switching current recorded by an ammeter and the results are shown in Fig. 3(a). It can be seen that the *anomalous* data points in the previous results as shown in Fig. 2(c) turn to be a smooth valley in the M-E curve, which has five key points denoted by letters I ~ V as shown in Fig. S4(a). This unusual and complicated valley corresponds to the domain reversal process as revealed by the PSR which has been divided into three stages C, D and E as shown in Fig. S4(a) and can be understood as following. At point I, the PMN-PT wafer is in a negatively poled rhombohedral phase with upward remnant polarizations $r1^{+}/r2^{+}$ as shown in Fig. S4(c). In this situation, the dominant polarizations $r1^{+}/r2^{+}$ make the easy axis of the FM film along the [100] direction and the magnetization keeps a large value as shown in state I in the middle panel of Fig. S4. When a small electric field (E = 1 kV/cm) was applied, the deformation of the rhombohedral polarization $r1'^{+}/r2'^{+}$ causes a slight elongated strain along the [100] direction (state II in the middle panel of Fig. S4), which produces a small enhancement of magnetization shown as point II in Fig. S4(a). Point I and point II are the start and end extremities of stage C and in this section the polarizations ($r1^{+}/r2^{+}$ or $r1'^{+}/r2'^{+}$) keep upward without any switching [Fig. S4(c)], as revealed by the PSR which keeps almost zero in Fig. S4(a). However, in the first half of stage D between point II to point III, the polarizations of PMN-PT begin to rotate remarkably and achieve an intermediate state at point III with polarizations r3/r4 dominant as shown in Fig. S4(d). The corresponding of point III in magnetization and intermediate state in polarization [Fig. S4(d)] is revealed by the PSR with the value of 50 % at point III as shown in Fig. S4(a). Since the polarizations r3/r4 deform the (011) plane significantly with compressive strain along the [100] direction and stretched strain along the [01-1] direction, the easy axis is rotated 90 ° as shown in stage III in the middle panel of Fig. S4. As a result, the magnetization along the [100] direction decreases sharply from about 980 emu/cm^3 to 600 emu/cm^3 as shown in Fig. S4(a) (from point II to point III). With further increased electric field in the other half of stage D between point III and IV, the

polarization reversal process continues and achieves the final domain state with downward polarizations $r1^{-}/r2^{-}$ [Fig. S4(e)] as revealed by the PSR which approaches 100 % at point IV in Fig. S4(a). The deformation induced by $r1^{-}/r2^{-}$ rotates the easy axis of magnetization back to the [100] direction as shown in stage IV in the middle panel of Fig. S4, and the magnetization increases to another larger value (point IV) as shown in Fig. S4(a). Further increase of the electric field in stage E between point IV and V causes the reorientation of polarization $r1^{'-}/r2^{'-}$ and continuous deformation of the (011) plane, resulting in decrease of magnetization and easy axis along the [01-1] direction as shown in stage V in the middle panel of Fig. S4. Notably, the magnetoelectric coupling is huge in stage D and has been considered very useful in terms of nonvolatile ME effect[2] and SME-RAMs[3]. However, relaxation behaviors has been observed in both halves of stage D by measuring the magnetization continuously at fixed electric fields of 1.5 kV/cm and 2.5 kV/cm respectively and the results are shown in Fig. S4(b). From the M-time and PSR-time curves, one can infer that the relaxation of magnetization is caused by the relaxation of domain switching and about 100 to 350 seconds are needed to reach a stable magnetization state. Therefore, electric field control of magnetization in the unipolar case without ferroelectric domain switching [Figs. 2(e) and 2(f) in the paper] should be preferred for the high-speed applications of SME-RAMs in the similar structures.

As a matter of fact, the polarization reversal process of the (011)-orientated PMN-PT is considerably complicated and mediated by rhombohedral, monoclinic (M) and orthorhombic (O) phases together[4-6]. The detailed images are described as following. The paraelectric phase of PMN-PT at high temperatures has a cubic symmetry, while the ferroelectric phase can be tetragonal (T, *P4mm*), rhombohedral (*R3m*) and orthorhombic (*mm2*) depending on the composition and temperature, with spontaneous polarization in <001>, <111> and <110> directions, respectively [Figures S5(a) and S5(b)]. Other phases (such as monoclinic phase) can also occur near morphotropic boundaries in the phase diagram when stress or electric

field is loaded. There are possibly three kinds of monoclinic phases, i.e. M_A, M_B and M_C among the rhombohedral, orthorhombic and tetragonal phases[4,5] as shown in Figs. S5(c) and S5(d). The monoclinic phases have been observed by optical method, and they are mediated phases in the polarization reversal process[6], as shown in Figs. S5(e) and S5(f).

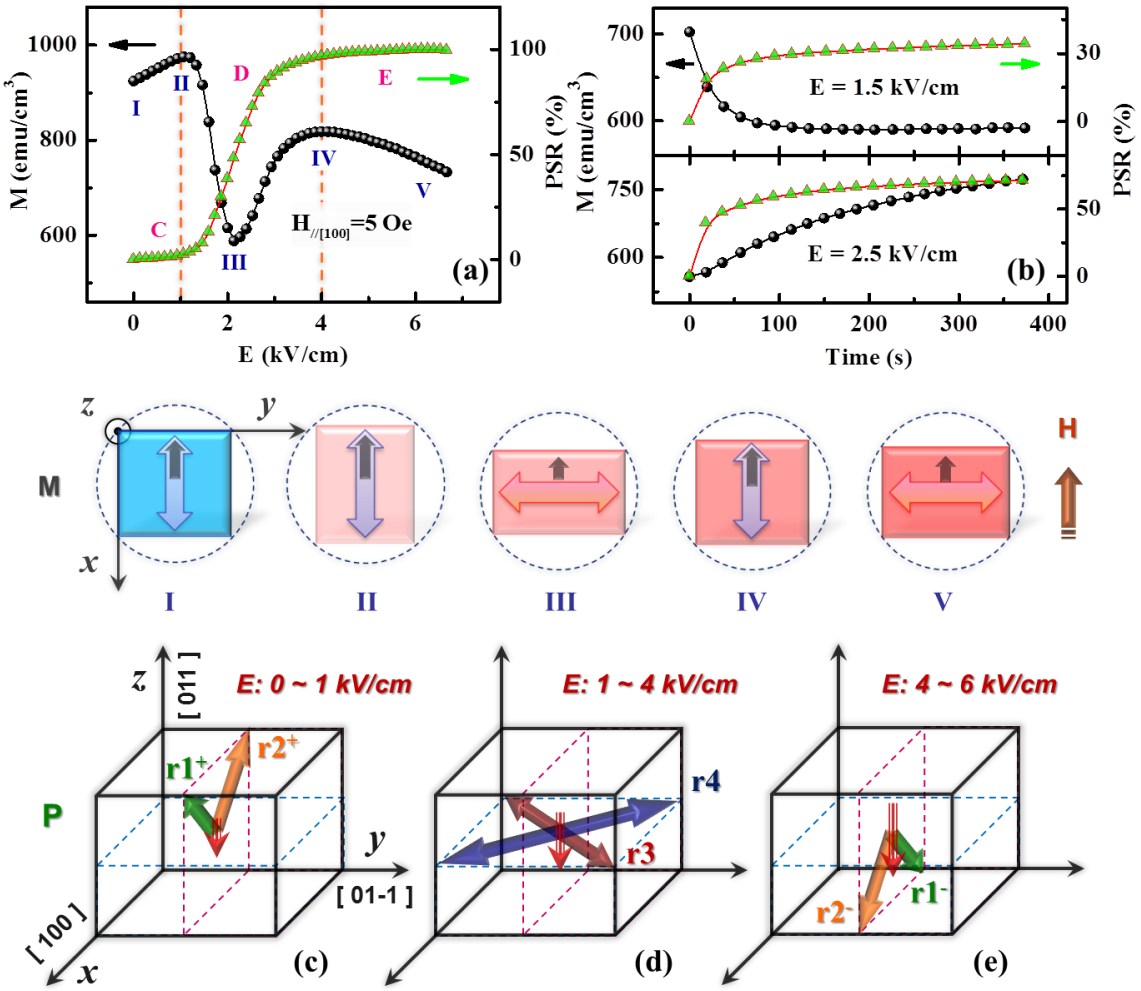

Figure S4 | Detailed jump process of magnetization tuned by polarization reversal in PMN-PT. (a) Expanded and fine M-E curve (black sphere) at low electric fields with $H_{//[100]}$ = 5 Oe, and the polarization switching ratio (PSR, green triangle) which has been acquired simultaneously. (b) Variation of magnetization (black sphere) and the corresponding PSR (green triangle) with time under electric fields of 1.5 kV/cm and 2.5 kV/cm under magnetic field of 5 Oe. The sketch in the middle panel describes the magnetization states (broad unidirectional arrows inside dashed circles), induced easy axis (broad bidirectional arrows),

deformation of the (011) crystal face (square) at different states corresponding to the magnetization states denoted by letters I ~ V in (a). (c) Body view of the unit cell and remnant polarizations of the PMN-PT of stage C after negatively poled states. (d) The unit cell and polarizations of the intermediate state with polarizations r3/r4 dominant during domain reversal process in stage D. (e) The unit cell and polarizations for stage E after domain reversal process .

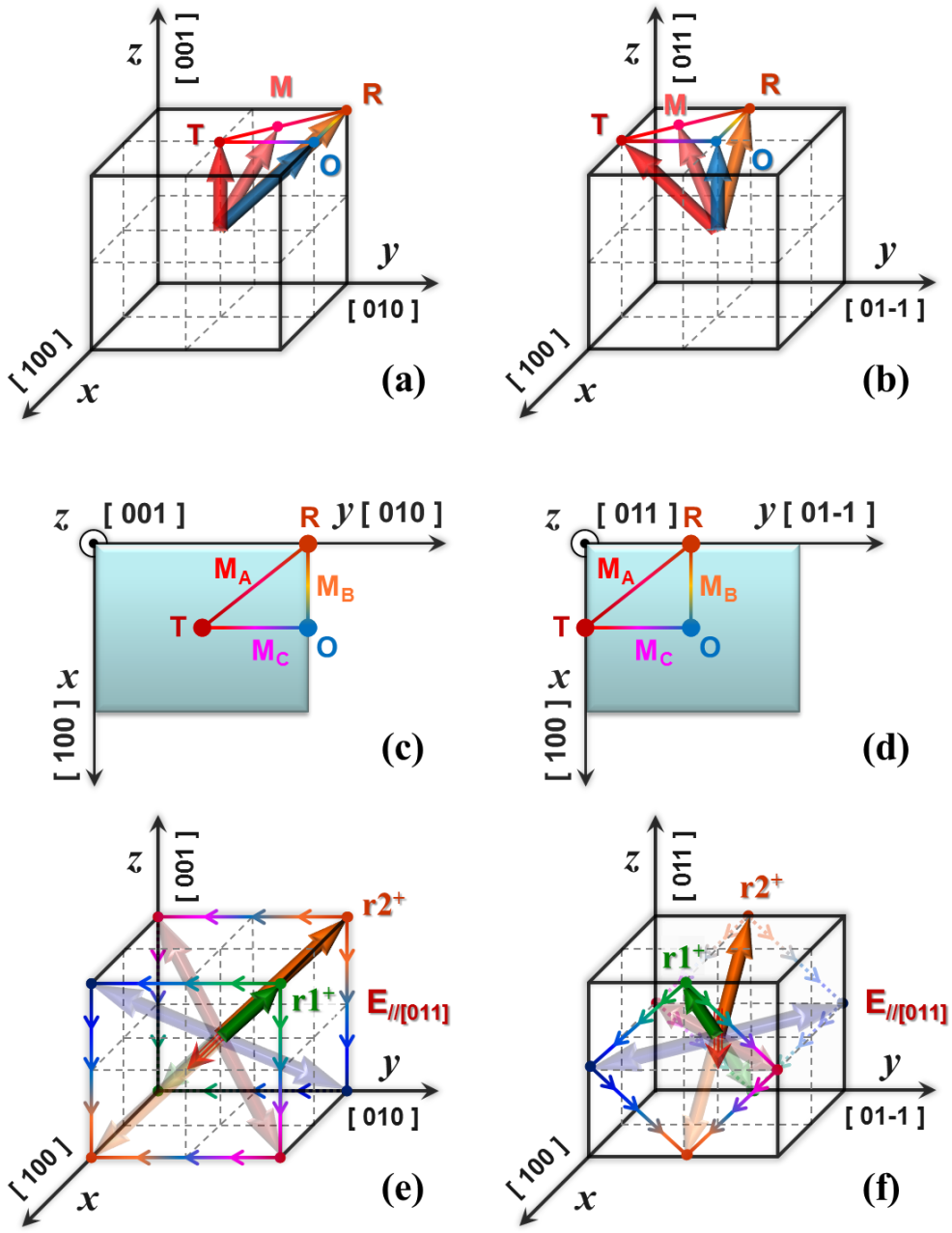

Figure S5 | The orientation of spontaneous polarization of different ferroelectric phase of PMN-PT near MPB and the polarization reversal process. (a) The orientation of spontaneous polarization of R, O, T and M phases in the (001)-cut case, as originally proposed by the previous reports (see Refs. 4 and 5). (b) The orientation of spontaneous polarization of R, O, T and M phases in the (011)-cut case. The spontaneous polarizations of M phase point at the lines between the spontaneous polarizations terminals of the R, O and T phases, by which method the M phase can be classified as M_A, M_B and M_C phases. (c) Top view of the spontaneous polarization of R, O, T and M_A, M_B, M_C phases in the (001)-cut case. (d) Top view of the spontaneous polarization of R, O, T and M_A, M_B, M_C phases in the (011)-cut case. (e) The (001)-view of polarization reversal process of PMN-PT mediated by R, M_B and O phases with electric field along the [011] direction, as originally proposed by the previous reports (see Refs. 6). (f) The (011)-view of polarization reversal process of PMN-PT mediated by R, M_B and O phases with electric field along the [011] direction. The small arrows in (e) and (f) are used to indicate the possible rotation paths of $r1^+$ and $r2^+$ during polarization reversal process.

Investigation of the electric-field control of magnetization in the unipolar case.

To eliminate the *anomalous* points in the M-E curves (i.e. Figs. 2(c) and 2(d) in the paper) which originate from the domain reorientation during polarization reversal process, a unipolar M-E measurement along the [100] direction with a small step of electric field was carried out. Since the M-E curves are almost symmetrical for the positive and negative voltages (Figure 2(c) in the paper), we mainly investigated the electric control of magnetization under positive unipolar electric fields. The sample was first poled by a positive electric field and then the M-E measurement was started with increasing positive electric field. The results are presented in Fig. S6(a), which shows a nonlinear M-E curve with small hysteresis, and the *anomalous*

points in the bipolar case (Figure 2(c) in the paper) disappear as expected since there is no polarization reversal process under unipolar electric fields. As a result, we can further analyze the tendency of magnetization tuned by electric field without the disturbance of the *anomalous* points. The unipolar M-E curve can be divided into four stages with every 5 kV/cm as denoted by the letters I ~ IV in the figure. In stage I (from 0 kV/cm to 5 kV/cm), the change of magnetization is slow and the variation is only about 120 emu/cm^3. The magnetization decreases sharply and largely in stage II (from 5 kV/cm to 10 kV/cm) with a change up to 430 emu/cm^3. However, the variation of magnetization slows down in stage III (from 10 kV/cm to 15 kV/cm) with a change of about 170 emu/cm^3. While in stage IV (from 15 kV/cm to 20 kV/cm), the change of magnetization is less than 20 emu/cm^3. What is more, the calculated magnetoelectric coupling coefficient ($\alpha=\mu_0 dM/dE$) [Figure S6(a)] can also be divided into four stages and a maximum value of ~1×10^{-6} s m^{-1} is achieved in stage II at about 7.5 kV/cm. In order to understand the behavior of the unipolar M-E curve, strain of the sample was measured along the [100] direction by using a strain gauge and the result is shown in Fig. S6(b). Similar to the previous report[7], the electric-field-induced strain (S-E curve) can be divided into three stages, as denoted by the letter C ~ E. In stage C (from 0 kV/cm to 10 kV/cm), the strain changes linearly with an in-plane piezoelectric constant ($d_{31}=dS/dE$) about -2000 pC N^{-1}. In stage D (from 10 kV/cm to 15 kV/cm), the slope of the S-E curve increases with a maximum absolute d_{31} value up to 2600 pC N^{-1}. As for stage E (from 15 kV/cm to 20 kV/cm), the variation of strain is minor and d_{31} is only about -200 pC N^{-1}.

Now, a key issue is to understand the origin of different stages in M-E and S-E curves and the correlation between them. The composition of PMN-PT used here is around the region of the MPB[1], which possess not only a ultra-high piezoelectric response but also has rich phase structures and ferroelectric domains. Due to the complexity of the phase composition and domain configuration near MPB, the domain reorientation and phase transformation can be easily induced by an external electric field, which has been proposed and observed in both the

(001)-cut[1,4] and the (011)-cut PMN-PT[5-7]. The three different stages in the strain curve [Figure S6(b)] correspond to three different ferroelectric phases, namely rhombohedral (R) phase in stage C, monoclinic phase (M_B) in stage D and orthorhombic (O) phase in stage E as shown in the lower panel of Figure S6. In stage C, the domain structure of PMN-PT is equivalent to the (011)-poled rhombohedral crystals [Figure S6(c)] and results in almost linear piezostrain behavior. With electric field increasing from 10 kV/cm to 15 kV/cm, the two equivalent <111>-orientated polarizations begin to tilt towards the [0-1-1] direction and M_B phase is induced [Figure S6(d)]. The polarization rotation of the M_B phase leads to a sharp change in strain and ultra-high piezoelectric constant as shown in stage D of Figure S6(b). For even higher electric fields (15 ~ 20 kV/cm), the domain structure of PMN-PT changes into monodomain state with polarization aligning in the [0-1-1] direction and induces the appearance of O phase [Figure S6(e)]. Since the orientation of polarization in the O phase is almost unchanged with increasing electric field, the variation of strain becomes saturated and the corresponding piezoelectric constant approaches zero in stage E.

Comparing the M-E and S-E curves in Figs. S6(a) and S6(b), it is easy to understand the correspondence of the turning points at 10 kV/cm and 15 kV/cm between the two curves. Moreover, the phenomenon that the tendency of the M-E curve changes to another stage at 5 kV/cm, while the change of the S-E curve keeps almost the same from zero to 10 kV/cm can also be understood by considering the Rot-MOKE in Fig. 3(d) of the paper, which makes the electric filed (5 kV/cm) to be the threshold where the easy axis of magnetization starts to rotate. Combining the results of electric-field-controlled magnetic anisotropy (Figure 3(d) in the paper) and the S-E curve [Figure S6(b)], the change of the unipolar M-E curves [Figure S6(a)] can be understood as following. At the beginning with E = 0, the crystal lattice of PMN-PT along the [100] direction is elongated due to the dominance of $r1^-/r2^-$ in R phase. As a result, the easy axis lies along the [100] direction [Figure S6(c)]. When electric fields are applied on the sample, compress strain is generated along the [100] direction as shown in Fig.

S6(b). However, according to the variation of magnetic anisotropy tuned by electric fields (Figure 3(d) in the paper), the easy axis keeps along the [100] direction below 5 kV/cm, resulting in slow change of magnetization. After the threshold of 5 kV/cm, the rotation of easy axis and continuous increase of piezostrain result in large magnetization change and maximum ME coupling coefficient. With further increase of electric field from 10 kV/cm, the ferroelectric state of rhombohedral PMN-PT has transformed to the M_B phase, which lead to ultra-high compressed strain. However, the rotation of magnetic easy axis has almost finished at 10 kV/cm, and the large strain is only to increase the amplitude of uniaxial magnetic anisotropy field (from 50 Oe to 120 Oe as shown in Fig. 3(d) of the paper). As a result, the magnetization decreases slowly. When the electric field is larger than 15 kV/cm, the ferroelectric state of PMN-PT translates into the O phase. Since the easy axis of magnetization has already lied along the [01-1] direction [Fig. S6(e)] and no more strain changes the amplitude of uniaxial magnetic anisotropy field [Fig. S6(b)], there is only a slight change of magnetization with ME coupling coefficient close to zero as shown in Fig. S6(a).

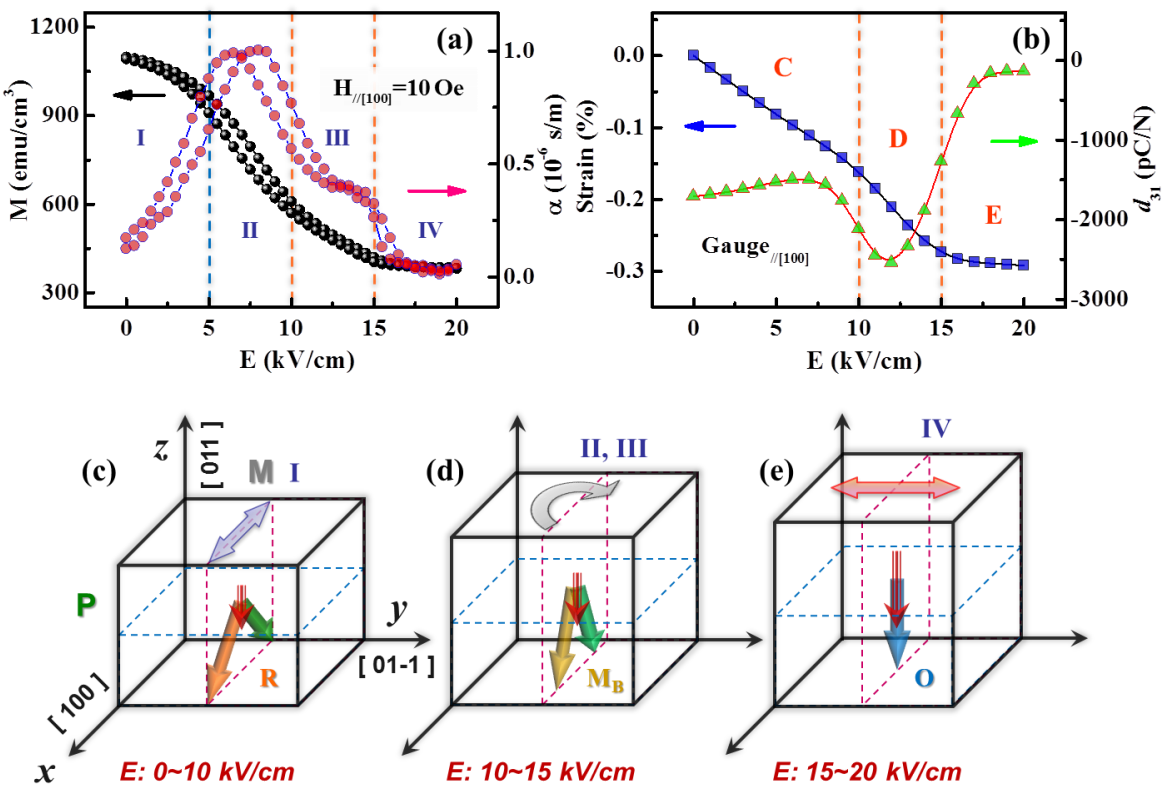

Figure S6 | Electric field induced ferroelectric phase transition and origin of the giant magnetization modulation. (a) Manipulation of magnetization (black sphere) by unipolar electric field with magnetic field 10 Oe and the calculated magnetoelectric coupling coefficient ($\alpha=\mu_0 dM/dE$, pink circle). (b) Strain (blue square) and deduced piezoelectric coefficient ($d_{31}=dS/dE$, green triangle) of PMN-PT under unipolar electric fields along the [100] direction. The three different stages of strain denoted by letters C ~ E in (b) correspond to the three different ferroelectric phases, namely R phase (c), M_B phase (d) and O phase (e) in the lower panel, and the four different stages of magnetization denoted by letters I ~ IV in (a) correspond to the four different magnetization states and orientations of the easy axis due to the three different ferroelectric phases tuned by electric fields.

Electric field control of magnetization characterized by Rot-MOKE method.

To investigate the magnetic anisotropy property of our sample under electric fields, Magnetic Optic Kerr Effect with a rotation-of-field (Rot-MOKE) and *in situ* electric field was employed. The structure of the sample used in the Rot-MOKE measurement is Ta(5 nm)/CoFeB(20 nm)/PMN-PT(0.2 mm)/Au(300 nm) as shown in Fig. S7(a), and the way of applying electric field is also shown there. In our experiment, the longitudinal effect of MOKE was used, where the magnetization vector is parallel to both the reflection surface and the plane of incidence. We can determine the magnetization by measuring the deflection angle of the polarization between incident light and reflected light, as shown in Fig. S7(b). The Rot-MOKE is based on the coherent rotation model, in which the sample is magnetized into a single domain state by a large magnetic field, and then the direction of external field is rotated step-by-step to carry out the MOKE measurements, as shown in Fig. S7(c).

For the case of pure uniaxial anisotropy[7], the gross energy density of the system is given by the following equation

$$E/V = -M_S H \cos(\theta-\varphi) + K_u \sin^2\varphi \quad (1)$$

Where E is the gross energy, V is the volume of the magnetic layer, M_S is the saturation magnetization, K_u is the uniaxial anisotropy constant, θ is the angle between external magnetic field and easy axis (EA), and φ is the angle between easy axis and magnetization. The direction of magnetization is determined by minimizing the total energy per unit volume, which results in the following equation

$$\partial(E/V)\partial\varphi = -M_S H \sin(\theta-\varphi) + K_u \sin 2\varphi = 0 \quad (2)$$

By defining torque $l(\varphi) = H \sin(\theta-\varphi)$, we obtain

$$l(\varphi) = H \sin(\theta-\varphi) = K_u \sin 2\varphi / M_S \quad (3)$$

As a result, uniaxial magnetic anisotropy can be identified by fitting the torque curve with the equation above.

In the Rot-MOKE experiment, the plane of incident light and reflected light was fixed in the (001) plane of the sample. Thus, the component of magnetization along the [01-1] (M_x) can be determined. After magnetizing the sample into a single domain state by a large magnetic field, the direction of the external magnetic field was rotated step-by-step. At each step, the value (H) and direction (θ) of the external field were acquired, and the direction of magnetization (φ) was deduced by $\cos(\varphi) = M_x/M_S$. Then, the magnetic torque moment $l(\varphi)$ was calculated by $H \cdot \sin(\theta-\varphi)$. After rotating the external magnetic field by a half circle, a torque curve can be gotten in terms of variation of the magnetic torque moment $l(\varphi)$ with angle φ, as shown in Fig. 3(b) in the paper. By repeating the torque measurement under a series of electric fields (i.e. from 0 kV/cm to 17.5 kV/cm, back to 0 kV/cm, then toward -17.5 kV/cm and finally back to 0 kV/cm), different torque curves were obtained and a quarter of them with electric field from 17.5 kV/cm to 0 kV/cm were shown in Fig. S7(d). Fitting all the results, variation of magnetic anisotropy with electric field was revealed (Figure 3(d) in the paper).

Since the diameter of the light spot in the MOKE measurement is only 0.2 mm, we can use it to investigate the local magnetization tuned by electric fields. Firstly, the magnetic

hysteresis loops under different electric fields were measured with the plane of incident light and reflected light fixed in the (01-1) plane. The squareness of the M-H loop is defined as M_r/M_S, and the variation of the M-H squareness with electric field is shown in Fig. S8(a). The normalized Kerr hysteresis loops at zero electric field and 15 kV/cm are shown in Figure S8(b). Secondly, the magnetic hysteresis loops under different electric fields were also measured with the optical plane fixed in the (001) plane, and the results are shown in Figs. S8(c) and S8(d). These local results are similar to that of MPMS measurement (Figure 2 in the paper), with a little enhancement of the converse ME effect (i.e. the change of squareness and the difference of M-H curves tuned by electric fields are more distinct).

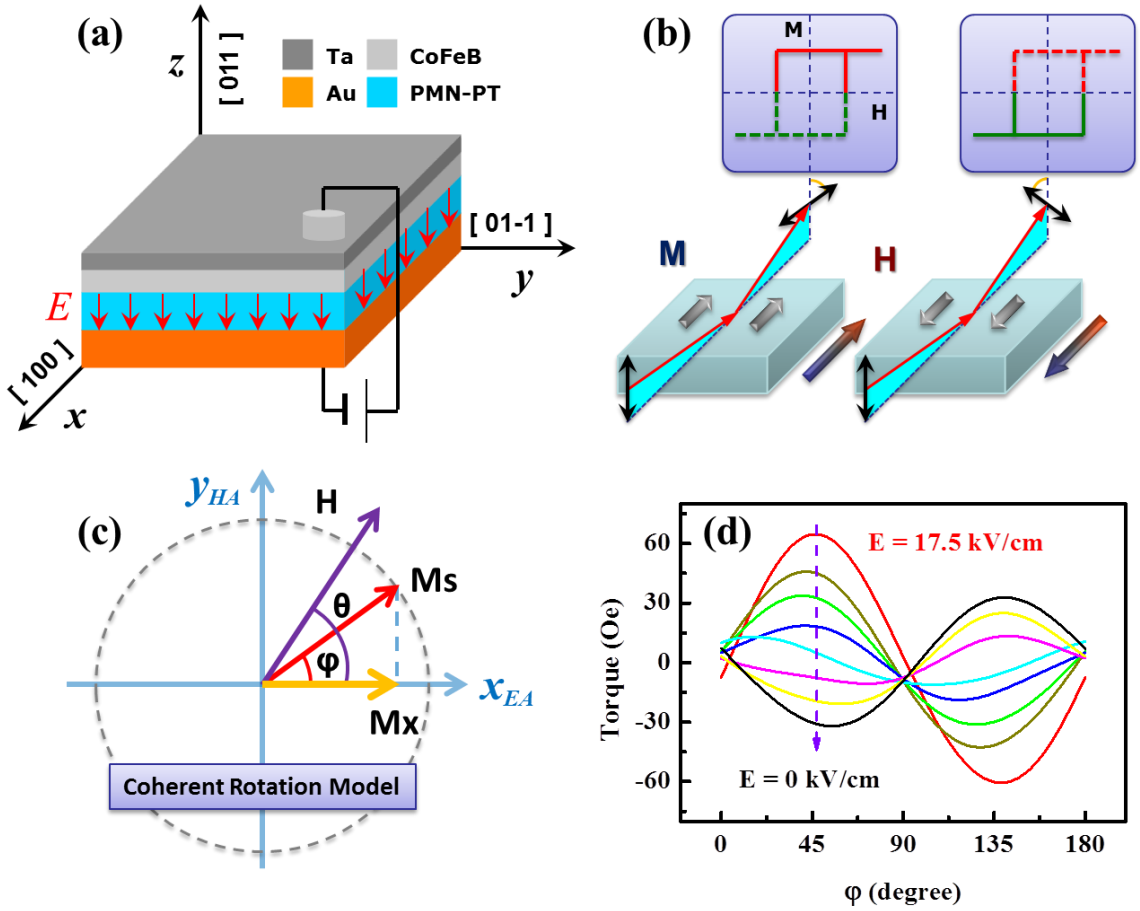

Figure S7 | Electric-field control of magnetic anisotropy characterized by Rot-MOKE method. (a) Structure of the sample and the configuration of measurement with applied electric field. (b) Operation process of the MOKE measurement and the acquisition of M-H curve. (c) Schematic of the MOKE measurement based on coherent rotation model. (d) Fitted

torque curves under different electric fields, form 17.5 kV/cm to zero with the decrement of 2.5 kV/cm.

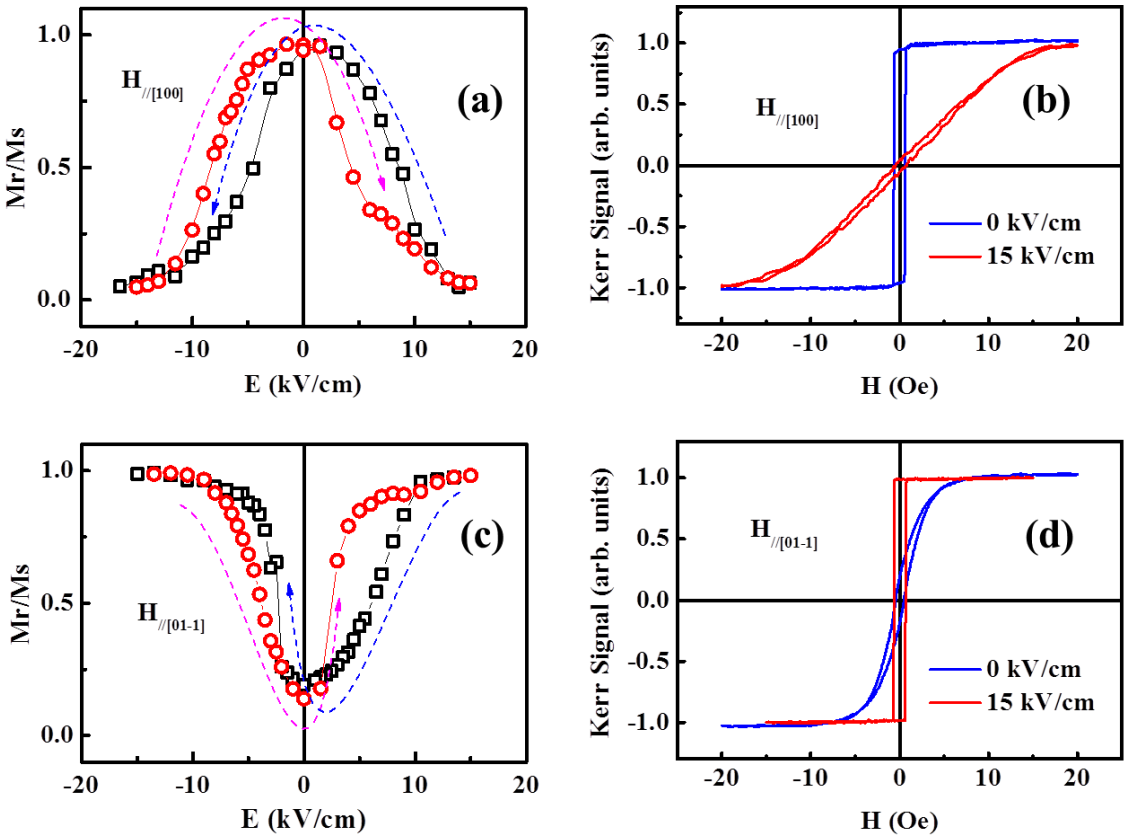

Figure S8 | Electric-field control of local magnetization characterized by MOKE method. (a) The squareness of the magnetic hysteresis loops (M_r/M_S) as a function of electric field along the [100] direction. (b) The normalized Kerr hysteresis loops along the [100] direction under electric field of 15 kV/cm (red line) and after removal of the electric field (blue line). (c) The squareness of the magnetic hysteresis loops (M_r/M_S) as a function of electric field along the [01-1] direction. (d) The normalized Kerr hysteresis loops along the [01-1] direction under electric field of 15 kV/cm (red line) and after removal of the electric field (blue line).

Theoretical calculation of the internal effective magnetic field induced by electric fields.

According to the method of calculation for strain induced magnetic field and relevant theories in the previous reports[9-11], the internal effective magnetic field induced by electric fields of the sample can be deduced as follows.

$$H_{eff} = 3\lambda_S (\sigma_{[100]} - \sigma_{[01\text{-}1]}) / M_S \quad (4)$$

Where H_{eff} is the internal effective magnetic field induced by the gross orthogonal piezo-stress along the two directions, i.e. $\sigma_{[100]}$, compressive stress along the [100] direction and $\sigma_{[01\text{-}1]}$, tensile stress along the [01-1] direction determined by the following equations.

$$\sigma_{[100]} = YE(d_{31}+\upsilon d_{32}) / (1-\upsilon^2) \quad (5)$$

$$\sigma_{[01\text{-}1]} = YE(d_{32}+\upsilon d_{31}) / (1-\upsilon^2) \quad (6)$$

Simplifying Eq. 4 by substituting Eqs. 5 and 6, we can get the final expression.

$$H_{eff} = 3\lambda_S YE(d_{31}-d_{32}) / (1+\upsilon)M_S \quad (7)$$

In which λ_S is the magnetostriction coefficient (31×10^{-6}), Y is the Young's modulus (1.6×10^{12} dyn cm^{-2}, CGS units), υ is the Poisson ratio (0.3), $4\pi M_S$ is the saturation magnetization (15000 Gs, CGS units) of the amorphous CoFeB layer, according to reports[12,13]. The in-plane piezoelectric coefficients of PMN-PT keep almost the same with the values of d_{31} ~ -2500 pC N^{-1} and d_{32} ~ 1400 pC N^{-1} when E < 7 kV/cm according to reports[7,14]. Hence, the induced internal effective magnetic fields at different electric fields can be calculated from Eq. 7 and the result is shown in Figure S9. Besides, different strain transfer efficiencies (STE) are considered in the calculation, and from the results one can see that 60 Oe effective magnetic field can be induced at 5 kV/cm when the STE is about 40 %. If further enhancing the STE by optimizing the samples, 60 Oe effective magnetic field can also be induced at 2 kV/cm on condition that STE ~ 80 %. However, it's hard to induce 60 Oe effective magnetic field with electric field below 1.5 kV/cm, as shown in the figure, for 60 Oe is the upper limit of effective magnetic field which can be induced by 1.5 kV/cm in this system with STE approaching 100 %. This theoretical calculation is useful in understanding the results of

electric control of magnetic anisotropy and helpful in optimizing the converse ME effect in the FM/FE heterostructures.

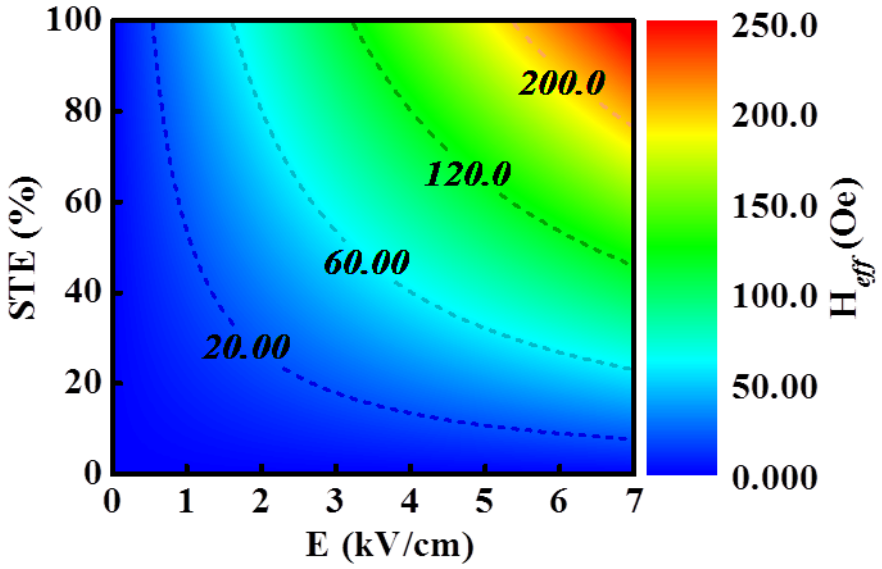

Figure S9 | Phase diagram of Electric field induced internal effective magnetic field with different stain transfer efficiencies. In the figure, the value of induced effective magnetic field can be easily found out with different colors (form blue to red). Three dashed curves labeled with the number 20, 60, 120 and 200 are the isolines of induced effective magnetic field with the value of 20 Oe, 60 Oe, 120 Oe and 200 Oe, respectively.

References

1. Park, S. E. & Shrout, T. R. Ultrahigh strain and piezoelectric behavior in relaxor based ferroelectric single crystals. *J. Appl. Phys.* **82**, 1804-1811 (1997).
2. Wu, T. *et al.* Giant electric-field-induced reversible and permanent magnetization reorientation. *Appl. Phys. Lett.* **98**, 012504 (2011).
3. Hu, J. M., Li, Z., Chen, L. & Nan, C. High-density magnetoresistive random access memory operating at ultralow voltage at room temperature. *Nat. Commun.* **2**, 533 (2011).

4. Fu, H. X. & Cohen, R. E. Polarization rotation mechanism for ultrahigh electromechanical response in single-crystal piezoelectrics. *Nature* **403**, 281-283 (2000).
5. Viehland, D. & Li, J. F. Anhysteretic field-induced rhombhohedral to orthorhombic transformation in <110>-oriented $0.7Pb(Mg_{1/3}Nb_{2/3})O_3$-$0.3PbTiO_3$ crystals. *J. Appl. Phys.* **92**, 7690-7692 (2002).
6. Fang, F., Yang, W. & Luo, X. [101]-oriented $Pb(Mg_{1/3}Nb_{2/3})O_3$-$PbTiO_3$ single crystals under electric loadings - polarization rotation linking M_B, O and R phases. *J. Am. Ceram. Soc.* **93**, 3916-3920 (2010).
7. Luo, L. *et al.* Ultrahigh transverse strain and piezoelectric behavior in (1-x)$Pb(Mg_{1/3}Nb_{2/3})O_3$-x$PbTiO_3$ crystals. *J. Appl. Phys.* **99**, 24104 (2006).
8. Mattheis, R. & Quednau, G. Determination of the anisotropy field strength in ultra-thin magnetic films using longitudinal MOKE and a rotating field: the ROTMOKE method. *J. Magn. Magn. Mater.* **205**, 143-150 (1999).
9. Lou, J., Liu, M., Reed, D., Ren, Y. H. & Sun, N. X. Giant electric field tuning of magnetism in novel multiferroic FeGab/lead zinc niobate-lead titanate (PZN-PT) heterostructures. *Adv. Mater.* **21**, 4711-4715 (2009).
10. Liu, M. *et al.* Giant electric field tuning of magnetic properties in multiferroic ferrite/ferroelectric heterostructures. *Adv. Funct. Mater.* **19**, 1826-1831 (2009).
11. Chen, Y. J. *et al.* Large converse magnetoelectric coupling in FeCoV/lead zinc niobate-lead titanate heterostructure. *Appl. Phys. Lett.* **94**, 082504 (2009).
12. Wang, D., Nordman, C., Qian, Z., Daughton, J. M. & Myers, J. Magnetostriction effect of amorphous CoFeB thin films and application in spin-dependent tunnel junctions. *J. Appl. Phys.* **97**, 10C906 (2005)
13. Jen, S. U. *et al.* Magnetic and electrical properties of amorphous CoFeB films. *J. Appl. Phys.* **99**, 053701 (2006).

14. Peng, J. *et al.* Orientation dependence of transverse piezoelectric properties of $0.70Pb(Mg_{1/3}Nb_{2/3})O_3$-$0.30PbTiO_3$ single crystals. *Appl. Phys. Lett.* **85**, 6221-6223 (2004).